Exploring the Composition Space of High Entropy Alloy Nanoparticles for the Electrocatalytic H₂/CO Oxidation with Bayesian Optimization

Vladislav A. Mints,[a] Jack K. Pedersen,[b] Alexander Bagger,[b] Jonathan Quinson,[b] [‡] Andy S. Anker,[b] Kirsten M. Ø. Jensen,[b] Jan Rossmeisl,[b] and Matthias Arenz [*a]

[a] University of Bern, Department of Chemistry, Biochemistry and Pharmaceutical Sciences, Freiestrasse 3, 3012 Bern, Switzerland

[b] University of Copenhagen, Department of Chemistry, Universitetsparken 5, 2100 Copenhagen Ø, Denmark

[‡] current address: Department of Biological and Chemical Engineering, Hangøvej 2 8200 Aarhus N, Denmark

[*] corresponding author, matthias.arenz@unibe.ch

Key Words: High entropy alloy nanoparticles; H2/CO oxidation reaction; Electrocatalysis; Machine Learning

Abstract: High entropy alloy (HEA) electrocatalysts offer a vast composition space that waits for exploration to identify interesting materials for energy conversion reactions. While first attempts have been made to explore the composition space of HEA thin film libraries and compare experimental and computational studies, no corresponding approaches exist for HEA nanoparticles. So far, catalytic investigations on HEA nanoparticles are limited to small sets of individual catalysts. Here, we report the experimental exploration of the composition space of carbon-supported Pt-Ru-Pd-Rh-Au nanoparticles for the H_2/CO oxidation reaction by constructing a dataset using Bayesian optimization as guidance. Applying a surfactant-free synthesis platform, a dataset of 68 samples was investigated. Constructing machine learned models, the relationship between the concentrations of the constituent elements and the catalytic activity was analyzed and compared to density functional theory (DFT) calculations. The machine learned models confirm findings from previous studies concerning the role of Ru for the H_2/CO oxidation reaction. This has been achieved starting from a random set of compositions and without any prior assumptions for the reaction mechanism nor any in-depth design of the active site. In addition, by comparing the trends of the computational and experimental studies, it is seen that the "onset potentials" across the compositions can be correlated with the adsorption energy of $^*OH$. The best correlation between the computational and experimental data is obtained when considering 5 % of the most strongly *OH adsorbing sites.

1 Introduction

Achieving a carbon neutral society through fossil fuel free technologies is one of the main challenges faced by mankind today. Within the scope of this challenge, the proton exchange membrane fuel cell has been developed.[1–3] In this specific fuel cell, electrocatalysts carry out the hydrogen oxidation reaction (HOR) and the oxygen reduction reaction (ORR) to generate electricity. The ORR is a major topic for studies as it requires large overpotentials to take place.[4] On the other hand, the HOR is efficiently catalyzed by Pt with negligible overpotentials.[5] However, Pt is highly susceptible to CO poisoning, i.e., the blocking of active sites for the HOR by adsorbed CO, whose traces are present in the hydrogen gas from the widely employed water gas shift reaction or potentially from on board methanol reformers.[6–8] Therefore, it is still an ongoing quest to find HOR catalysts that show resilience towards CO poisoning.[9]

A common strategy to increase the CO tolerance of Pt is to alloy it with Ru.[10] This produces a bifunctional catalyst that can perform both the HOR and the CO oxidation at low overpotentials.[11] The proposed mechanism for PtRu mediated catalysis is that ruthenium facilitates the formation of adsorbed OH species at lower potentials.[12] These adsorbed OH species can oxidize the CO adsorbed on Pt which leads to the re-activation of the surface. In addition, it has been proposed that an electronic effect of Ru weakens the CO bond on Pt.[13] Studies on alloy catalysts are conventionally limited to bi- and trimetallic alloys. However, recently HEAs emerged as potential catalyst materials for electrocatalytic energy conversion reactions.[14–18] HEAs contain five or more elements in a randomized order, which produces a surface with multiple different active sites.[19] Further, the diversity of elements with different sizes distorts the crystal lattice which gives HEAs not only unique mechanical properties but also a tunable electronic structure.[20] The statistical nature of the HEA surface compositions is not only expected to provide unique catalytic properties that have yet to be explored.[21] Furthermore, the comparison of activity trends in the HEA composition space observed in

experiment with results from computational investigations enables a unique approach for improved insight into catalytic reactions.

Experimental investigations of HEAs form a major challenge due to the vast composition space. In a HEA containing five elements there are $99!/(95!4!) = 3,764,376$ compositions possible when each elemental concentration is varied between 1 and 96 at.% (atomic percent) in steps of 1 at.%. Neither can this many compositions be investigated experimentally in a timely manner, nor can it be expected that the majority of compositions exhibit interesting catalytic properties. Consequently, new strategies to approach the study and discovery of relevant HEAs with dedicated properties are necessary.[22,23] Currently, one approach is focused on constructing a methodology employing density functional theory (DFT) that enables prediction of highly active HEA compositions, which then are evaluated experimentally in the form of thin film libraries.[24,25] Such investigations can be combined with machine learning tools to guide an efficient exploration of the composition space.[26,27] In addition to the potential discovery of new materials of high activity, the comparison of activity trends in the computational model with trends observed in experiments potentially allows new approaches of understanding catalytic reactions. In contrast to thin film libraries that allow compositional gradients, studies with HEA nanoparticles are particular demanding. The compositions are discrete instead of continuous and not all compositions can necessarily be synthesized. Furthermore, catalysts employed in fuel cells typically need to be supported onto a high surface area carbon, which complicates the synthesis. For this reason, to the best of our knowledge so far, no studies have been reported for the machine learning guided exploration of the composition space of carbon-supported HEA nanoparticles for electrocatalytic reactions.

Here we present an experimental strategy guided by Bayesian optimization to explore the composition space of carbon-supported HEA nanoparticles for electrocatalytic energy conversion reactions. The conceptual design of the study is summarized in Scheme 1. Using a surfactant-free synthesis platform[28,29], carbon-supported Pt-Ru-Pd-Rh-Au nanoparticles are

4

prepared starting from a random set of compositions and experimentally tested for the electrocatalytic H₂/CO oxidation reaction. The ratio of the precursor mixtures was used as the input parameter for a Bayesian optimization algorithm, whereas a defined CO oxidation "onset potential" in the presence of H₂ served as the output parameter to describe the H₂/CO oxidation activity. As the well-defined precursor mixtures not necessarily result in defined nanoparticle compositions, in a second part, machine learned models were constructed with a new input parameter, namely the compositions of the as-prepared nanoparticles determined from energy dispersive X-ray spectroscopy (EDS). Finally, the correlations were related to physical phenomena using DFT models. In a predictive model, we compared the trends in the observed "onset potentials" to the weighted sum of normally distributed *OH adsorption energies giving insight in the required number of active sites for CO oxidation site reaction in the HOR.
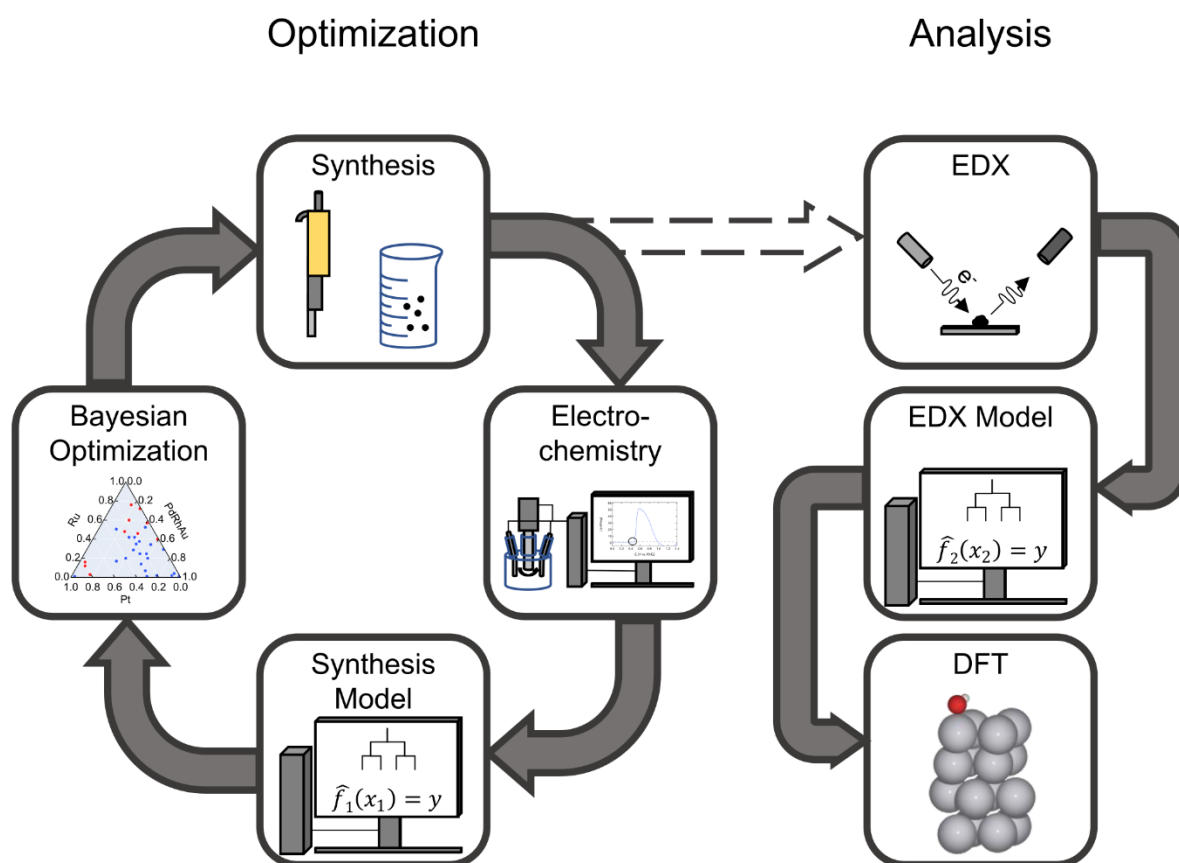
Scheme 1. Schematic representation of the optimization loop and the analysis steps.

2 Experimental

5

2.1 Catalyst Synthesis

The solid precursors, H_2PtCl_6 (Sigma Aldrich, 99.9%) $HAuCl_3$ (Alfa Aesar, 99.99%) $RuCl_3$ (Sigma Aldrich, ReagentPlus), $PdCl_2$ (Sigma Aldrich, ReagentPlus, 99%), and $RhCl_3$ (Sigma Aldrich, 99.98%) were dissolved in methanol (Merck, EMSURE) to produce 20 mM precursor solutions. A total of 1 mL of precursor solutions were added in stoichiometric ratios to 5.6 mL 57 mM NaOH MeOH with 50 wt.% (metal to carbon) dispersed high surface area carbon support (Vulcan XC72R). The obtained solution was stirred for ten minutes at room temperature and stored overnight in a centrifuge tube. The following day, the suspensions were centrifuged, decanted and left to dry in air. Catalyst inks were prepared by adding isopropanol and H_2O (3:1, v/v) to the dry catalyst powder to produce a 0.83 mg metal per mL ink. These inks were drop casted onto a glassy carbon RDE tip to produce a metal loading of 35 μg cm^{-2}.

2.2 Electrochemistry

All experiments were carried out in a three electrode RDE setup. In between experiments, the electrochemical cell and all glass components were stored in 1 g mL^{-1} $KMnO_4$ acidified with H_2SO_4. Before the experiments, this solution was removed and residual MnO_2 was dissolved by adding a dilution of $H2SO_4$ and H_2O_2. Following, the electrochemical cell and components were boiled three times in MilliQ water.

All measurements were carried out with a Nordic Potentiostat EC200. As a reference electrode a trapped RHE electrode was employed. A platinum wire separated by a glass frit was used as a counter electrode. The electrolyte was 0.1 M H_2SO_4 (Merck Suprapur). The working electrode consisted of a Radiometer RDE which has a glassy carbon disk on which the catalyst containing ink was drop casted. This working electrode was put under controlled potential of 0.05 V vs. RHE into the solution. In the first 30 seconds CO gas (Air Liquide, Quality 37) was bubbled through the electrolyte which was followed by 10 cyclic voltammograms (CVs) between 0 and 0.6 V vs. RHE at a scan speed of 100 mV s^{-1}. After, the electrode was kept for 2 minutes longer at 0.05 V vs. RHE in CO atmosphere. Next, the solution was degassed for 20 minutes with H_2

(ALPHAGAZ, 99.999%) and 2 CVs were recorded between 0 and 1.4 V vs. RHE at a scan speed of 10 mV s^{-1}.

2.3 EDS and TEM analysis

The samples for EDS were prepared by dropcasting several times 10 μL of catalyst ink onto a copper foil to yield a thick catalyst film. The EDS measurement were performed in a GeminiSEM450 (Zeiss), operated with Smart SEM 6.05, using the EDS Photodetector Ultim max 65 (Oxford instruments), operated with AZTec 4.2. The EDS spectra were measured at four different locations with a size of 800 μm^2 at a working distance of 8 mm and an accelerating voltage of 25 kV. The transmission electron microscopy (TEM) samples were prepared by dropcasting once the catalyst ink on a copper grid. TEM micrographs and their associated EDS spectra were acquired on a JEOL 2100 TEM operated at 200 kV.

2.4 Machine learning

2.4.1 Dataset construction

The dataset for the different Pt-Ru-Rh-Pd-Au alloy compositions was constructed in a Bayesian manner similar to the research of Nugraha et al.[26] The first 25 data points were selected randomly but they included the 5 "extreme" compositions that span the domain of interest. These "extreme" HEA compositions consisted of 96% of one element and 1% of each remaining element. The electrochemistry for the CO oxidation was evaluated using the HOR as a probe reaction. Subsequently, only particles that remained active for the HOR after the CO got oxidized were included into machine learning. This resulted in an initial dataset containing a total of 21 points. The input parameter for the machine learning models were the precursor ratios used in the synthesis as this is the most defined parameter. The output parameter was the CO oxidation "onset potential". This potential was defined at a current increase of 1.5 mA mg^{-1} on top of the capacitive current. For every synthesized alloy, 3 electrochemical experiments were carried out.

This obtained information was used to construct a random forest regression model using the python package scikit learn.[30] The parameters, n estimatros, bootstrap, max depth, max features, min sample leaf, min sample_split, criterion, were tuned using 500 Bayesian optimization cycles which optimized the k-fold cross validation score. All Bayesian Optimization loops made use of the GpyOpt library in python.[31] The obtained random forest regression model was further used to find new alloy compositions of interest for investigation. It was optimized using Bayesian optimization, in which the first iteration consisted of the compositions that were used to train the model initially. This way, the Bayesian optimization constructed the prior probability distribution using the same data that were acquired from laboratory experiments. Following, the Bayesian optimization was continued for an additional 50 iterations, in which new compositions were suggested for evaluation. From these 50 compositions, 10 compositions were selected based on their Euclidian distance in space to other suggested or studied compositions and their predicted activity. Subsequently, these 10 samples were synthesized, evaluated, and added to the optimization. The expansion of the dataset was halted after 5 optimization cycles, as the mean absolute error (MAE) of the leave one out cross validation (LOOCV) showed to reach a constant value around 13 mV. This suggested that an exponential amount of data is becoming necessary to improve the models. In addition, the target of finding the best performing alloy was reached in the first cycle. In the end, this resulted in a dataset of 68 unique catalysts. The scripts used in this paper together with the final data set are available on https://github.com/vamints/Scripts_BayesOpt_PtRuPdRhAu_paper.

After the catalysts were analyzed with EDS, new input parameters were obtained, which corresponded to elemental ratios observed by EDS. These allowed to construct a new random forest model, which used the same hyperparameter tuning script as the synthesis model. All random tree models were explained using the SHAP package.[32]

2.4.2 Linear models

Linear models were constructed using the scikit learn package. Features were expanded to include also polynomial terms up to the second degree. The best Lasso Regression model was selected by using a custom loop that varied the lambda penalty until the change in lambda was less than 1%. The ternary contour plots were created by using the plotly library.[33] The models were fitted using the entire dataset of 68 experimental points. Following these models were used to predict the values of a grid, that spanned the slice of the hyperspace that is shown in the contour plot.

2.5 DFT calculations

DFT calculations were done with the GPAW code[34,35] version 19.8.1 and the revised Perdew-Burke-Ernzerhof (RPBE) exchange-correlation functional.[36] Manipulation of atomic structures was performed with the Atomic Simulation Environment (ASE).[37] Four-layered face-centered cubic (fcc) (111) surface slabs measuring 2x2 atoms laterally, and periodically repeated laterally from orthogonal unit cells, were constructed for each of the constituent elements Au, Pd, Pt, Rh, and Ru for $*$OH adsorption energy calculations. The surface slabs were constructed with fcc lattice constants that were obtained as the minimum energy lattice parameters for the pure fcc bulk constituents (see

Table 1).

Table 1: Fcc lattice constants and $*$OH adsorption free energies of the pure elements used

Metal	Au	Pd	Pt	Rh	Ru
DFT fcc lattice constant (Å)	4.2149	3.9814	3.9936	3.8648	3.8285
DFT ΔG_{*OH} (eV)	1.30	0.80	0.76	0.44	0.04

During structure relaxations all but the two top layers of the slab were fixed, and the $*$OH adsorbate was put at on-top positions with the oxygen atom constrained to move only

perpendicular to the surface. The slabs were constructed with a vacuum of 15 Å above and below the structure. The wave functions were expanded in plane waves with an energy cut-off of 500 eV, and sampling of the Brillouin zone was done on a Monhorst-pack grid of k-points sized 8x8x1. The structures were relaxed so that the maximum force on any atom did not exceed 0.05 eV/ Å. For other parameters, the default parameters of GPAW were used.

*OH adsorption free energies were calculated relative to the *OH adsorption energy on Pt(111) which has been shown to adsorb *OH about 0.1 eV stronger[38] than the maximum of the oxygen reduction reaction (ORR) activity volcano at 0.86 eV relative to $H_2O(l)$ and $H_2(g)$,[39] i.e. setting the free energy of *OH adsorption on Pt(111) to about 0.76 eV.

$$\Delta G_{*OH} = \left(E_{*OH} - E_*\right) - \left(E_{*OH}^{Pt(111)} - E_*^{Pt(111)}\right) + 0.76 \ eV$$

Here, ΔG_{*OH} is the free energy of *OH adsorption, E_{*OH} and E_* are the DFT calculated energies of the surface slab with and without *OH adsorbed, respectively. The adsorption energies used in this work are given in

Table **1**.

3. Results and Discussion

To explore the composition space of HEA nanoparticles, we developed a simple and straightforward approach that was adopted from our surfactant-free colloidal synthesis method using alkaline mono-alcohols optimized for mono- and bimetallic nanomaterials.[28,29,40,41] Here, we take advantage of the room temperature reduction of $HAuCl_4$ in alkaline methanol[42] to initiate the particle formation and the reduction of multicomponent precursor in solutions and in the presence of a high surface area carbon support. The alkaline methanol serves as reducing agent,[42] whereas the presence of the carbon support limits the formation of macroscopic Au particles. Nevertheless, relatively large Au nanoparticles were formed (< 20 nm) when only a single Au precursor was used, whilst the presence of multiple precursors comprising elements

like Pt, Ir, Ru, Rh, and Pd, leads to a very fast reaction at room temperature, as demonstrated in Figure S1, and the formation of small, supported nanoparticles. Using a combination of TEM and EDS analysis, it is shown that the formed nanoparticles are ca. 3 nm in diameter and incorporate all the precursor metals, i.e., Pt, Ru, Pd, Rh, and Au, see Figure 1 and Figure S2. The particle size is only slightly larger than monometallic Pt or Ir nanoparticles obtained in alkaline methanol by heating[28,43,44] and is ideal for achieving a high active surface area. On the other hand, the small particle size inhibits the verification of a single phase with random elemental composition by XRD or high-resolution STEM-EDX.
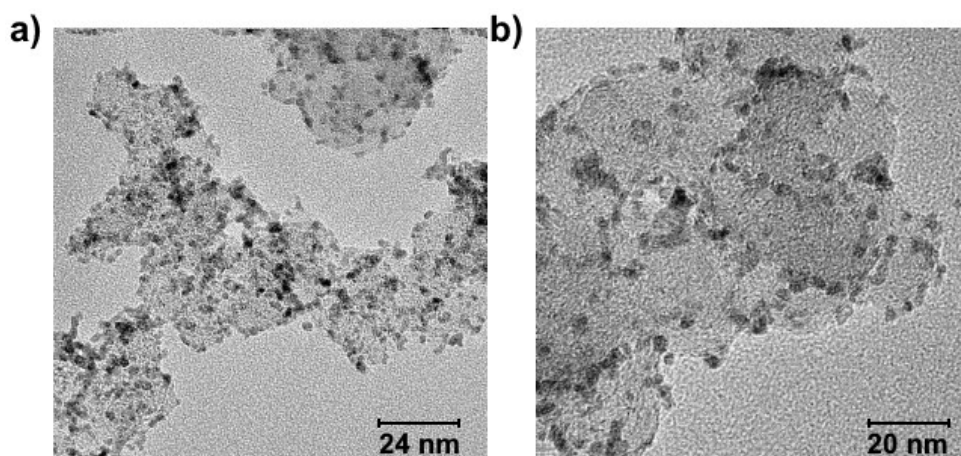

Figure 1: a-b) TEM micrographs of the sample $Pt_{12}Ru_{38}Pd_8Rh_{41}Au_1$.

To explore and optimize the composition of the Pt-Ru-Pd-Rh-Au nanoparticles for the electrocatalytic H_2/CO oxidation reaction, 25 samples were selected as starting point for the Bayesian optimization,[26,27] whereof 20 were selected randomly and 5 were selected close corner points of the composition space. To obtain a well-defined output parameter as a measure for the H_2/CO oxidation activity in the optimization process, a CO oxidation "onset potential" was defined. For this, first a saturated CO monolayer was deposited on the nanoparticles, which was subsequently electrochemically oxidized by a potential scan in an H_2 rich environment using a rotating disk electrode (RDE) configuration. The HOR thereby amplified the potential at which the CO monolayer was oxidized by a rapid increase in current for the catalysts that are active

for the HOR. The CO "onset potential" was then defined as the potential where an increase of 1.5 mA $mg^{-1}_{PtRuPdRhAu}$ on top of the capacitive current was measured, see Figures S3 and S4.
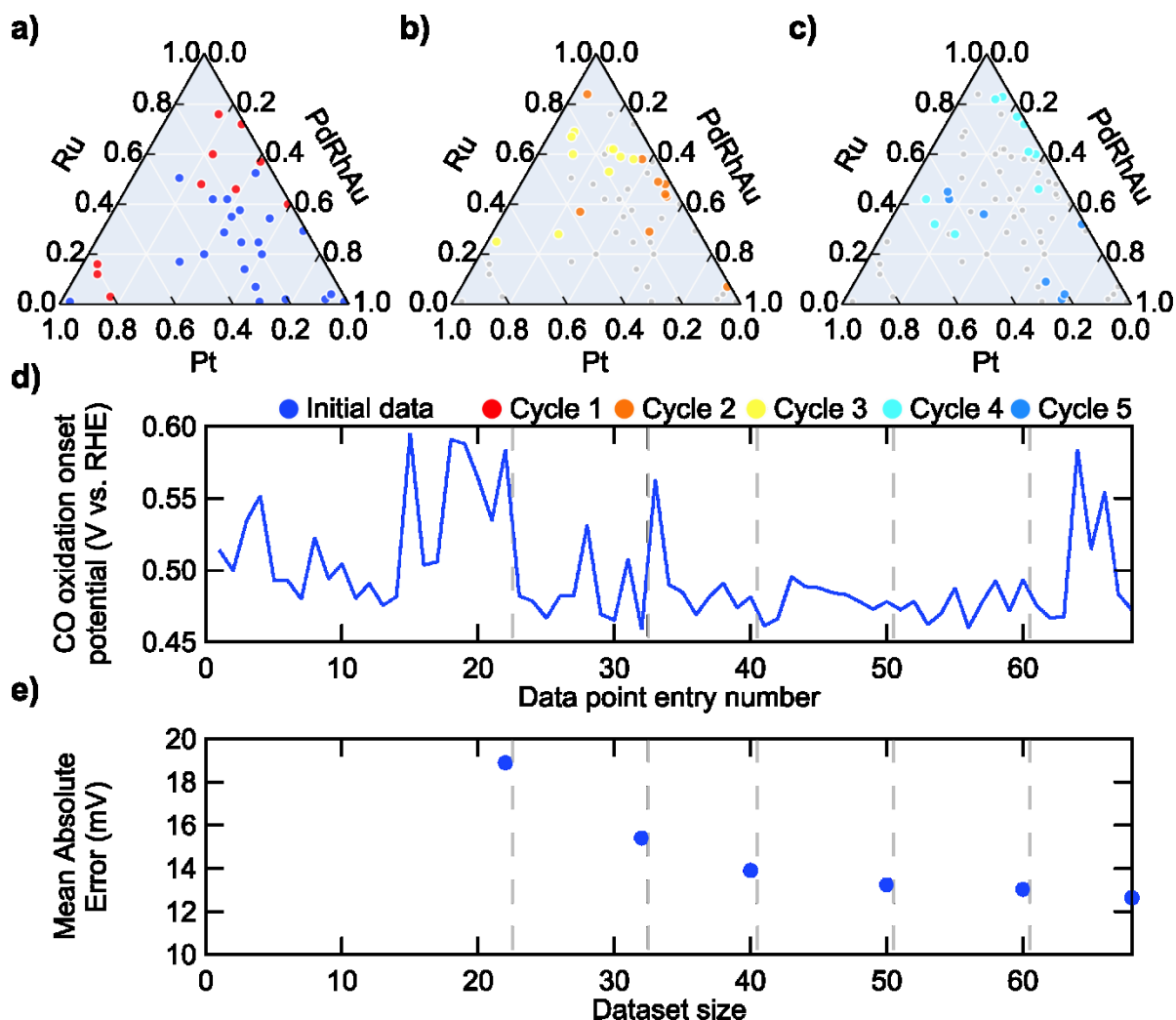

Figure 2: **a-c)** Representation of the precursor mixtures that were used to synthesize the particles in each Bayesian optimization cycle. **d)** The experimentally determined CO oxidation onset potential for each data point in the investigated order. The dashed lines indicate the regions of each Bayesian optimization cycle. **e)** The change in the mean absolute error, obtained from the leave-one-out cross-validation method of the synthesis random forest regression model with each Bayesian optimization cycle.

Feeding the experimental results of the initial 25 samples to the Bayesian optimization process which was performed in conjunction with a random forest regression model, 10 new compositions were suggested, which were experimentally investigated and added to the dataset. This addition of 10 new samples concludes a single optimization cycle. In total five optimization cycles were carried out, which results are summarized in Figure 2. It can be observed that after the second optimization cycle, the computational methods start to select

12

samples with large Ru content. Figure 2d shows the average CO oxidation onset potentials for the investigated samples. It can be seen that the most active catalyst composition, with a precursor ratio of $Pt_{16}Ru_{46}Pd_2Rh_{34}Au_2$, was found within the first optimization cycle at the 32nd entry. The actual composition of this alloy, determined by EDX, was $Pt_{12}Ru_{38}Pd_8Rh_{41}Au_1$. In the subsequent 2nd, 3rd and 4th cycles the onset potentials mainly stay around 0.47 V vs. RHE. Furthermore, in the 3rd-5th cycle the Bayesian optimization suggests on average large Ru contents. Thus, it can be implied that Ru is playing a major role in the CO oxidation reaction. In the 5th cycle, several low performing compositions were selected for investigation, to explore further poorly represented regions. This exploration produced samples with low CO tolerance, in line with the prediction, and suggests that the optimization has already found the most active composition in the first cycle. Finally, the evolution of the synthesis random forest regression models can be studied in Figure 2e represented by the mean absolute error (MAE), which was calculated with leave-one-out cross-validation (LOOCV). The MAE shows an exponential decrease with increasing dataset size, the final synthesis model having a MAE of 13 mV.

While the precursor ratios serve as an excellent input parameter for the Bayesian optimization procedure, they might poorly reflect the true catalyst compositions. Thus, the obtained correlations between the precursor ratios and the CO oxidation onset might not be as informative as required to understand in more depth the composition-activity relationship of the investigated catalysts. Therefore, all sampled catalysts were investigated with EDX to determine their actual composition. The results were used to construct two intrinsically different machine learned models, here referred to as *EDX models*.
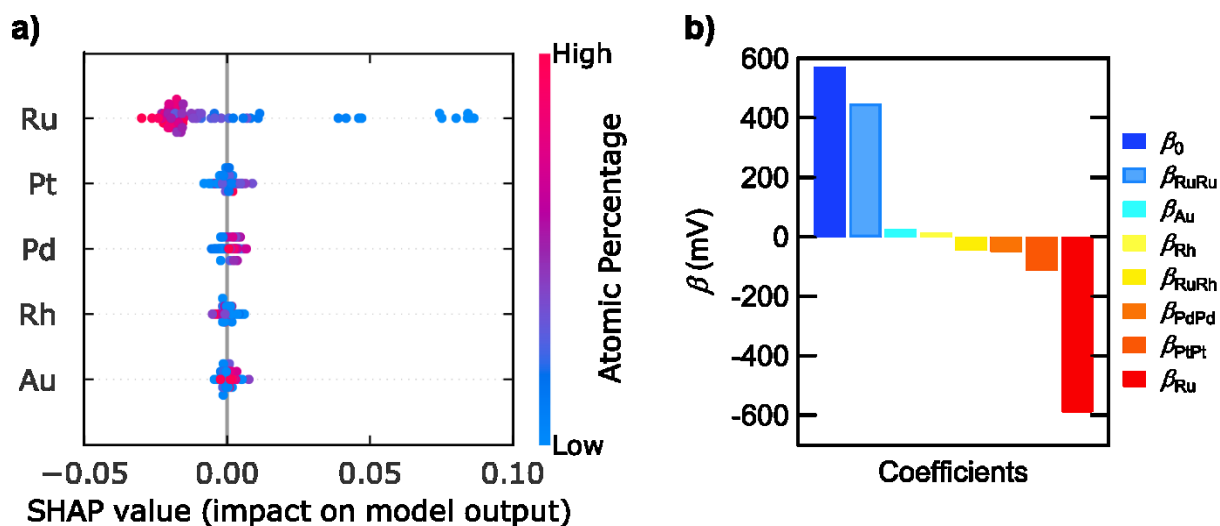
Figure 3: **a)** SHAP analysis of the EDX random forest regression model. **b)** The coefficients of EDX Lasso regression model.

The first model was a EDX random forest regression, which is highly flexible in its nature as it has no bias on the expected correlations. An interpretation of the model was achieved using SHapely Additive exPlanation (SHAP), the results of which are shown in Figure 3a.[32,45] The SHAP value represents the perturbation of the CO oxidation "onset potential" by the element from the average onset potential. Hence negative SHAP values are associated with a decrease in overpotential for the CO oxidation. It turns out that of the investigated elements, Ru has the largest impact on the CO oxidation. In low quantities Ru exhibits a very large positive SHAP value and at large quantities a negative SHAP value. This is congruent with the already reported activity of Ru towards CO oxidation being much higher compared to the other investigated metals.[46] The next elements that show to improve the CO oxidation in large quantities are Pt and Rh. These two metals have also been shown to oxidize the CO monolayer at higher potentials compared to Ru, however at lower potentials than Pd.[47] In contrast to Ru, Pt, and Rh, large quantities of Pd showed to increase the CO oxidation onset potential, relative to the average, as shown in Figure 3a. Au, in comparison to the other elements, did not show to have a large impact on the H_2/CO oxidation. This could be explained by a different mechanism for the formation of the CO monolayer on Au. While CO forms a stable chemisorbed monolayer

14

on Pt, Pd, Rh, and Ru, this not the case for Au in a CO deficient environment.[48] In addition, Au is inactive for the HOR.[49]

The second model is a more rigid linear model, which was limited to the first- and second-degree polynomial terms to avoid overfitting with higher degree terms. The obtained coefficients were corrected to account for the statistical probability of finding a specific elemental arrangement at the surface. This model is outlined in Equation 1 and can be used for a discussion of the active surface sites for the H_2/CO oxidation reaction. In equation 1, $E(X)$ is the CO oxidation onset potential, f is the fraction of an element m in at.%, β is the fitted coefficient, $P(X = m)$ is the probability of finding an element at the surface, $P(X = m_1 m_2)$ is the probability of finding two neighboring elements. Nevertheless, this model has a total of 21 predictors, which would severely overfit the small dataset of 68 points by using the ordinary least squares regression. Therefore, to reduce the amount of predictors, the model was fitted using the lasso regression.[50]

$$E(f_{Pt}, f_{Ru}, f_{Pd}, f_{Rh}, f_{Au}) = \beta_0 + \sum_i \beta_{m_i} P(X = m_i) + \sum_{i \geq j} \beta_{m_i m_j} P(X = m_i m_j)$$

$$P(X = m_i) = 0.5 f_{m_j} \tag{1}$$

$$P(X = m_i m_j) = \begin{cases} f_{m_i} f_{m_j} & \text{if } i > j \\ 0.5 f_{m_i} f_{m_j} & \text{if } i = j \end{cases}$$

The terms of the lasso regression with their coefficients can be observed in Figure 3b. Similar to the random forest model, the lasso regression shows that the term $P(X = Ru)$ has the largest associated negative coefficient. Therefore, Ru has the biggest impact on reducing the onset potential. In addition, linear models show that $P(X = RuRu)$ has a large associated positive coefficient. This suggests that there is an optimum amount of Ru in an alloy, i.e., too much Ru limits the activity for the H_2/CO oxidation. The next term that improves the H_2/CO oxidation is

15

P(X = PtPt), which is also in agreement with the random forest model. When the linear model is used to predict the performance for a Pt-Ru alloy, an optimum is found around the $Ru_{52}Pt_{48}$ composition. This composition overlaps with previous studies that observed a similar maximum for this binary alloy.[51,52] Finally, the lasso regression includes the terms: *P(X = Rh)*, *P(X = Au)*, *P(X = RuRh)*, *P(X = PdPd)* in the fit. However, their coefficients are too small to draw a solid conclusion upon.
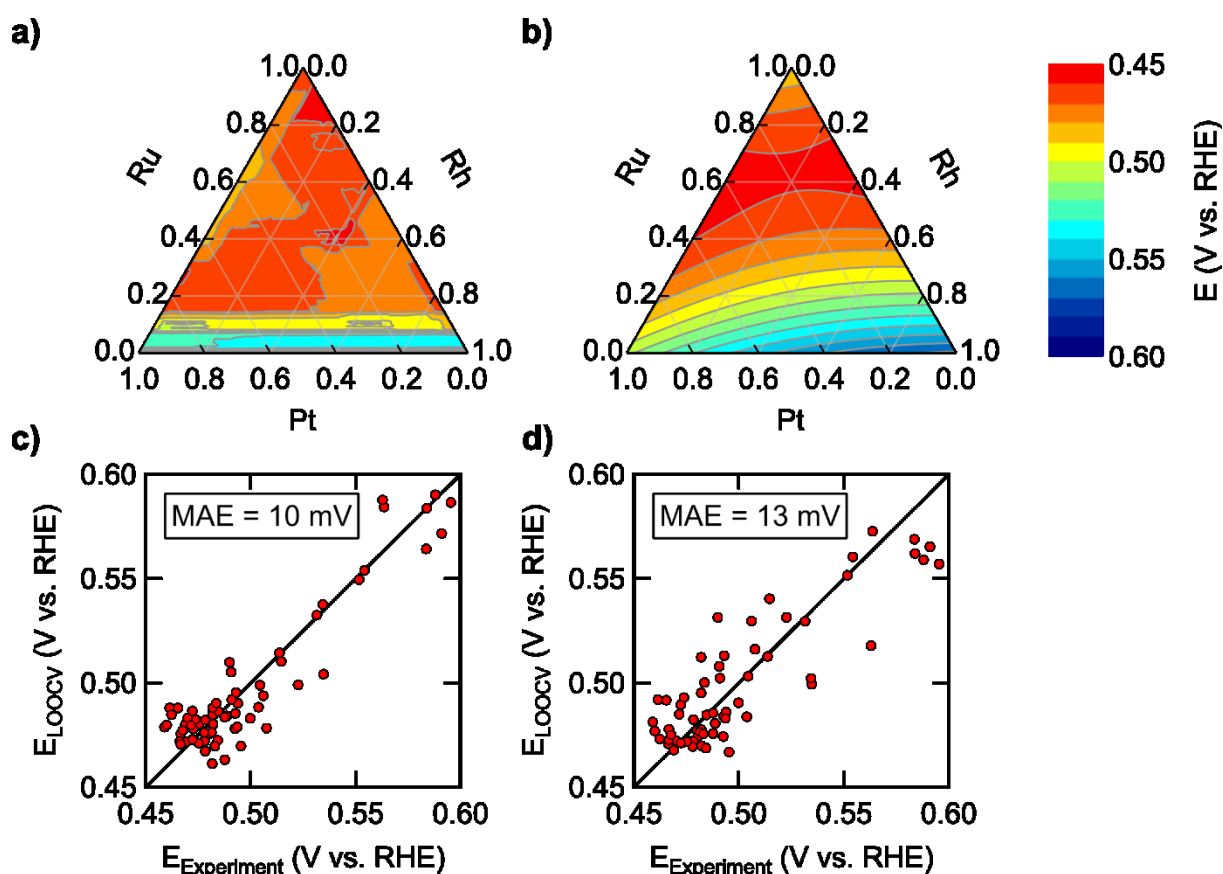

Figure 4: **a-b)** The slice of the hyperspace spanned by Ru, Pt and Rh and **c-d)** the prediction of the LOOCV vs the experimental value of the models: **a,c)** EDX Random Forest Regression **b,d)** EDX Lasso Regression.

The analysis of the SHAP values calculated on the EDX model concluded that among the investigated five elements Ru, Pt and Rh are lowering the CO oxidation "onset potential" the most. This allows a visualization of the activity of this hypothetical Ru-Pt-Rh ternary alloy. In Figure 4a and b, the CO oxidation onset potential of the Ru-Pt-Rh alloys are predicted using

the EDX random forest regression and EDX lasso regression respectively. Both models show that there is not a single most active alloy, but different composition regions which contain alloys that exhibit similar high H_2/CO oxidation activities. The shapes of these regions differ between the two EDX models due to their intrinsic flexibility. The lasso regression assumes a quadratic relationship, which produces straight and smooth boundaries for the maximum domain. In comparison, the random forest regression has no prior bias, which produces domains with an irregular boundary. However, both models show relative broad composition regions of high activity facilitating the fast identification of active catalysts in the Bayesian optimization. Finally, the performance of the two EDX models was compared using the MAE of the LOOCV. This evaluation is shown in Figure 4c-d The EDX random forest regression model outperforms the lasso regression slightly with an MAE of 10 mV. This is highly correlated with the high flexibility of the model. On the other hand, the lasso regression has an MAE of 13 mV. It should be noted that the investigated compositions were selected using an optimization algorithm, which focused mainly on samples in the high-performance region. As observed, this region consists mostly of alloys with large concentrations of Ru. Therefore, the models in this study can predict the activity of catalysts that fall into the Pt-Ru-Pd-Rh-Au space with large Ru quantities. However, the error increases for alloys with little to no Ru content.

To gain further physical understanding of the modelled composition-activity relationships, DFT simulations were conducted. The task of finding the limiting step of the reaction enabling HOR is formidable given that the surface structures of the nanoparticle catalysts are not well defined. Additionally, the many possible adsorption sites on the HEA nanoparticle surface contribute to an inherent complexity in the variation of active sites. This further hinders a successful and timely discovery of the responsible chemical step. Instead, we pursued a predictive model which could explain the trend in the observed onset potentials through electronic structure insights. The model considers the weighted sum of normally distributed *OH adsorption energies with means given by the pure metal constituents of the HEA and with standard

deviations set to 0.13 eV as observed previously for *OH adsorption energy distributions on a comparable HEA.[19] The molar fractions of each element in the compositions found with EDX of each HEA constituted the weights of each of the normal distributions in the linear combination given by Equation 2. Here, P is the resulting distribution of *OH adsorption energies, ΔG_{*OH}, for a given HEA composition. f_m is the molar fraction of metal m, μ_m is the adsorption energy obtained for the pure metal m, and $\sigma = 0.13$ eV is the spread in the adsorption energies.

$$P\left(\Delta G_{*OH}\right) = \sum_{m}^{metals} f_m N\left(\Delta G_{*OH}; \mu_m, \sigma\right) = \sum_{m}^{metals} f_m \frac{1}{\sqrt{2\pi}\sigma} e^{-\frac{1}{2}\left(\frac{\Delta G_{*OH}-\mu_m}{\sigma}\right)^2} \qquad (2)$$
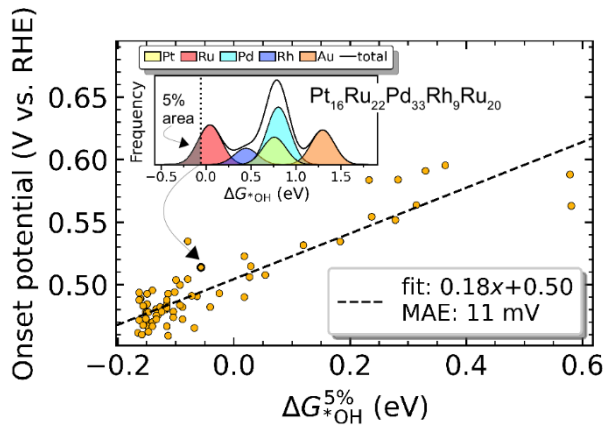

Figure 5: Correlation of experimental onset potentials with the *OH adsorption energy at the 5 percentile of most strongly bound sites of the *OH adsorption energy distribution for the EDX-analyzed compositions. The inset shows an example of the modeled *OH adsorption energy distribution for an HEA sample. The 5 percentile *OH adsorption energy is found as the energy at which 5% of the area of the distribution is to the left.

Figure 5 shows the overall predictive trend obtained by the computationally inexpensive model. The best fit between the experimentally obtained onset potential and the computational model is obtained using the adsorption energy at the 5 percentile of most strongly adsorbing sites in the modeled *OH adsorption energy distributions for each of the sampled HEA compositions, see the trend line in Figure 5. The 5 percentile of most strongly adsorbing sites was chosen

since it was found to constitute a minimum in the prediction error compared to other possible percentiles (see Figure S13).

A somewhat linear relationship can be observed with a capability of predicting onset potentials with an MAE of 11 mV, comparable to the machine learning models. This observed trend indicates that the oxidation of water at the catalyst surface and subsequent formation of oxygen adsorbed intermediates are involved in the potential-limiting step. Although the *OH adsorption energy seems a good descriptor for the overall trend of the onset potential across a large span of *OH adsorption energies, there is a substantial variance for the sampled Ru-rich compositions with strong *OH adsorption at around -0.1 eV that is not explained by the simple model and calls for more in-depth investigations. In other words, this simple model is not able to predict the details of highly performing catalysts. In contrast to the experimental results, the simple model predict pure Ru as the most active catalyst. It is expected that a more advanced model needs to take into account the CO adsorption energy as well. Nevertheless, comparing the trends from experimental investigations and computational studies over a large composition space of supported multi-element nanoparticles indicates that a relatively small number of surface sites with high *OH adsorption energy is sufficient to determine the catalytic activity of the nanoparticle catalysts.

4. Conclusions

In this research, the composition space of Pt-Ru-Pd-Rh-Au nanoparticles was optimized for the H$_2$/CO oxidation reaction using Bayesian optimization. Starting from a synthesis with a random set of precursor compositions and experimentally testing the electrocatalytic H$_2$/CO oxidation activity, a guided search among the vast number of different compositions is achieved. The most active alloy was found within the first optimization cycle, after 32 experiments. Subsequent cycles provided mostly alloys within the high-performance region, with only several exploration points in the low performance region. The results are obtained without an

in-depth characterization of the samples that would have been very time consuming and difficult due to the very small particle size. Thus, it remains unresolved if all catalysts with high performance can be considered high entropy alloys.

In a step further, the obtained dataset was used to scrutinize the composition-activity relationship of the H_2/CO oxidation reaction. This was achieved by constructing a random forest regression and a lasso regression. In good agreement with previous studies, both models point out that Ru is the key element in the CO oxidation reaction. The models show that Ru should be present in the nanoparticle neither at too low nor at too high concentrations. Using the lasso regression to predict the performance for a bimetallic Pt-Ru alloy, a similar optimum in composition is found to what has been reported to be the best performing Pt-Ru catalyst. These results strongly indicate that the presented strategy of using a simple, surfactant-free synthesis as well as an optimization process with minimal characterization of the nanoparticle catalyst that relies mainly on well-defined synthesis variables and introduces a measure for the catalytic performance is an effective strategy to explore the vast composition space of HEA nanoparticle catalysts. This becomes in particular important when including further metals to the composition space.

Last but not least, comparing the experimental results of the trend in onset potential with DFT calculations, the relationships were shown to correlate with the *OH adsorption energy. These are lowest for Ru. Therefore, within this composition space, sufficient amounts of Ru are obligatory for a high performing CO oxidation catalyst. The best fit between DFT calculations and experimental results is obtained when considering for each of the sampled HEA compositions the adsorption energy at the 5 percentile of most strongly adsorbing sites in the modeled *OH adsorption energy distributions. This indicates that a relative low number of strongly adsorbing *OH sites are sufficient for a rough prediction of the performance of a H_2/CO oxidation catalyst. In conclusion, the presented study outlines an efficient and feasible

approach for the exploration of multidimensional composition spaces of carbon-supported, multi-component nanoparticles combining experimental and computational means.

Supporting Information

Synthesis procedure, TEM of particles, Data processing procedure, CVs from particles, MEA of DFT models at different at.% percentiles

References

(1)   Andújar, J. M.; Segura, F. Fuel Cells: History and Updating. A Walk along Two Centuries. *Renew. Sustain. Energy Rev.* **2009**, *13* (9), 2309–2322. https://doi.org/10.1016/j.rser.2009.03.015.

(2)   Rath, R.; Kumar, P.; Mohanty, S.; Nayak, S. K. Recent Advances, Unsolved Deficiencies, and Future Perspectives of Hydrogen Fuel Cells in Transportation and Portable Sectors. *Int. J. Energy Res.* **2019**, *43* (15), 8931–8955. https://doi.org/10.1002/er.4795.

(3)   Alaswad, A.; Omran, A.; Sodre, J. R.; Wilberforce, T.; Pignatelli, G.; Dassisti, M.; Baroutaji, A.; Olabi, A. G. Technical and Commercial Challenges of Proton-Exchange

Membrane (PEM) Fuel Cells. *Energies* **2020**, *14* (1), 144.
https://doi.org/10.3390/en14010144.

(4)   Gasteiger, H. A.; Kocha, S. S.; Sompalli, B.; Wagner, F. T. Activity Benchmarks and Requirements for Pt, Pt-Alloy, and Non-Pt Oxygen Reduction Catalysts for PEMFCs. *Applied Catalysis B: Environmental*. 2005, pp 9–35. https://doi.org/10.1016/j.apcatb.2004.06.021.

(5)   Gasteiger, H. A.; Panels, J. E.; Yan, S. G. Dependence of PEM Fuel Cell Performance on Catalyst Loading. *J. Power Sources* **2004**, *127* (1–2), 162–171. https://doi.org/10.1016/j.jpowsour.2003.09.013.

(6)   Jackson, C.; Raymakers, L. F. J. M.; Mulder, M. J. J.; Kucernak, A. R. J. Poison Mitigation Strategies for the Use of Impure Hydrogen in Electrochemical Hydrogen Pumps and Fuel Cells. *J. Power Sources* **2020**, *472* (April), 228476. https://doi.org/10.1016/j.jpowsour.2020.228476.

(7)   Zheng, T.; Zhou, W.; Li, X.; You, H.; Yang, Y.; Yu, W.; Zhang, C.; Chu, X.; San Hui, K.; Ding, W. Structural Design of Self-Thermal Methanol Steam Reforming Microreactor with Porous Combustion Reaction Support for Hydrogen Production. *Int. J. Hydrogen Energy* **2020**, *45* (43), 22437–22447. https://doi.org/10.1016/j.ijhydene.2020.06.107.

(8)   Gurau, V.; Ogunleke, A.; Strickland, F. Design of a Methanol Reformer for On-Board Production of Hydrogen as Fuel for a 3 KW High-Temperature Proton Exchange Membrane Fuel Cell Power System. *Int. J. Hydrogen Energy* **2020**, *45* (56), 31745–31759. https://doi.org/10.1016/j.ijhydene.2020.08.179.

(9)   Uchida, H.; Izumi, K.; Watanabe, M. Temperature Dependence of CO-Tolerant Hydrogen Oxidation Reaction Activity at Pt, Pt-Co, and Pt-Ru Electrodes. *J. Phys. Chem. B* **2006**, *110* (43), 21924–21930. https://doi.org/10.1021/jp064190x.

(10)   Koper, M. T. M. Electrocatalysis on Bimetallic and Alloy Surfaces. *Surf. Sci.* **2004**,

548 (1–3), 1–3. https://doi.org/10.1016/j.susc.2003.10.045.

(11)   Freitas, K. S.; Lopes, P. P.; Ticianelli, E. A. Electrocatalysis of the Hydrogen Oxidation in the Presence of CO on RhO2/C-Supported Pt Nanoparticles. *Electrochim. Acta* **2010**, *56* (1), 418–426. https://doi.org/10.1016/j.electacta.2010.08.059.

(12)   Watanabe, M.; Furuuchi, Y.; Motoo, S. Electrocatalysis by AD-Atoms. Part XIII. Preparation of Ad-Electrodes with Tin Ad-Atoms for Methanol, Formaldehyde and Formic Acid Fuel Cells. *J. Electroanal. Chem.* **1985**, *191* (2), 367–375. https://doi.org/10.1016/S0022-0728(85)80029-2.

(13)   Buatier de Mongeot, F.; Scherer, M.; Gleich, B.; Kopatzki, E.; Behm, R. . CO Adsorption and Oxidation on Bimetallic Pt/Ru(0001) Surfaces – a Combined STM and TPD/TPR Study. *Surf. Sci.* **1998**, *411* (3), 249–262. https://doi.org/10.1016/S0039-6028(98)00286-6.

(14)   Yeh, J. W.; Chen, S. K.; Lin, S. J.; Gan, J. Y.; Chin, T. S.; Shun, T. T.; Tsau, C. H.; Chang, S. Y. Nanostructured High-Entropy Alloys with Multiple Principal Elements: Novel Alloy Design Concepts and Outcomes. *Adv. Eng. Mater.* **2004**, *6* (5), 299–303. https://doi.org/10.1002/adem.200300567.

(15)   Zou, Y.; Ma, H.; Spolenak, R. Ultrastrong Ductile and Stable High-Entropy Alloys at Small Scales. *Nat. Commun.* **2015**, *6* (1), 7748. https://doi.org/10.1038/ncomms8748.

(16)   Ye, Y. F.; Wang, Q.; Lu, J.; Liu, C. T.; Yang, Y. High-Entropy Alloy: Challenges and Prospects. *Mater. Today* **2016**, *19* (6), 349–362. https://doi.org/10.1016/j.mattod.2015.11.026.

(17)   Wu, D.; Kusada, K.; Yamamoto, T.; Toriyama, T.; Matsumura, S.; Kawaguchi, S.; Kubota, Y.; Kitagawa, H. Platinum-Group-Metal High-Entropy-Alloy Nanoparticles. *J. Am. Chem. Soc.* **2020**, *142* (32), 13833–13838. https://doi.org/10.1021/JACS.0C04807.

(18)   Nellaiappan, S.; Katiyar, N. K.; Kumar, R.; Parui, A.; Malviya, K. D.; Pradeep, K. G.; Singh, A. K.; Sharma, S.; Tiwary, C. S.; Biswas, K. High-Entropy Alloys as Catalysts

for the CO2 and CO Reduction Reactions: Experimental Realization. *ACS Catal.* **2020**, *10* (6), 3658–3663. https://doi.org/10.1021/acscatal.9b04302.

(19)   Batchelor, T. A. A.; Pedersen, J. K.; Winther, S. H.; Castelli, I. E.; Jacobsen, K. W.; Rossmeisl, J. High-Entropy Alloys as a Discovery Platform for Electrocatalysis. *Joule* **2019**, *3* (3), 834–845. https://doi.org/10.1016/j.joule.2018.12.015.

(20)   Xin, Y.; Li, S.; Qian, Y.; Zhu, W.; Yuan, H.; Jiang, P.; Guo, R.; Wang, L. High-Entropy Alloys as a Platform for Catalysis: Progress, Challenges, and Opportunities. *ACS Catal.* **2020**, *10* (19), 11280–11306. https://doi.org/10.1021/acscatal.0c03617.

(21)   Löffler, T.; Savan, A.; Garzón-Manjón, A.; Meischein, M.; Scheu, C.; Ludwig, A.; Schuhmann, W. Toward a Paradigm Shift in Electrocatalysis Using Complex Solid Solution Nanoparticles. *ACS Energy Lett.* **2019**, *4* (5), 1206–1214. https://doi.org/10.1021/acsenergylett.9b00531.

(22)   Yao, Y.; Liu, Z.; Xie, P.; Huang, Z.; Li, T.; Morris, D.; Finfrock, Z.; Zhou, J.; Jiao, M.; Gao, J.; Mao, Y.; Miao, J. (John); Zhang, P.; Shahbazian-Yassar, R.; Wang, C.; Wang, G.; Hu, L. Computationally Aided, Entropy-Driven Synthesis of Highly Efficient and Durable Multi-Elemental Alloy Catalysts. *Sci. Adv.* **2020**, *6* (11), eaaz0510. https://doi.org/10.1126/sciadv.aaz0510.

(23)   Ludwig, A. Discovery of New Materials Using Combinatorial Synthesis and High-Throughput Characterization of Thin-Film Materials Libraries Combined with Computational Methods. *npj Comput. Mater. 2019 51* **2019**, *5* (1), 1–7. https://doi.org/10.1038/s41524-019-0205-0.

(24)   Batchelor, T. A. A.; Löffler, T.; Xiao, B.; Krysiak, O. A.; Strotkötter, V.; Pedersen, J. K.; Clausen, C. M.; Savan, A.; Li, Y.; Schuhmann, W.; Rossmeisl, J.; Ludwig, A. Complex-Solid-Solution Electrocatalyst Discovery by Computational Prediction and High-Throughput Experimentation**. *Angew. Chemie Int. Ed.* **2021**, *60* (13), 6932–6937. https://doi.org/10.1002/anie.202014374.

(25)   Pedersen, J. K.; Batchelor, T. A. A.; Bagger, A.; Rossmeisl, J. High-Entropy Alloys as Catalysts for the CO2 and CO Reduction Reactions. *ACS Catal.* **2020**, *10* (3), 2169–2176. https://doi.org/10.1021/ACSCATAL.9B04343.

(26)   Nugraha, A. S.; Lambard, G.; Na, J.; Hossain, M. S. A.; Asahi, T.; Chaikittisilp, W.; Yamauchi, Y. Mesoporous Trimetallic PtPdAu Alloy Films toward Enhanced Electrocatalytic Activity in Methanol Oxidation: Unexpected Chemical Compositions Discovered by Bayesian Optimization. *J. Mater. Chem. A* **2020**. https://doi.org/10.1039/d0ta04096g.

(27)   Pedersen, J. K.; Clausen, C. M.; Krysiak, O. A.; Xiao, B.; Batchelor, T. A. A.; Löffler, T.; Mints, V. A.; Banko, L.; Arenz, M.; Savan, A.; Schuhmann, W.; Ludwig, A.; Rossmeisl, J. Bayesian Optimization of High-Entropy Alloy Compositions for Electrocatalytic Oxygen Reduction**. *Angew. Chemie - Int. Ed.* **2021**, *60* (45), 24144–24152. https://doi.org/10.1002/anie.202108116.

(28)   Quinson, J.; Neumann, S.; Wannmacher, T.; Kacenauskaite, L.; Inaba, M.; Bucher, J.; Bizzotto, F.; Simonsen, S. B.; Theil Kuhn, L.; Bujak, D.; Zana, A.; Arenz, M.; Kunz, S. Colloids for Catalysts: A Concept for the Preparation of Superior Catalysts of Industrial Relevance. *Angew. Chemie - Int. Ed.* **2018**, *57* (38), 12338–12341. https://doi.org/10.1002/anie.201807450.

(29)   Quinson, J.; Kacenauskaite, L.; Bucher, J.; Simonsen, S. B. S. B.; Theil Kuhn, L.; Oezaslan, M.; Kunz, S.; Arenz, M. Controlled Synthesis of Surfactant-Free Water-Dispersible Colloidal Platinum Nanoparticles by the Co4Cat Process. *ChemSusChem* **2019**, *12* (6). https://doi.org/10.1002/cssc.201802897.

(30)   Pedregosa, F.; Varoquaux, G.; Gramfort, A.; Michel, V.; Thirion, B.; Grisel, O.; Blondel, M.; Prettenhofer, P.; Weiss, R.; Dubourg, V.; Vanderplas, J.; Passos, A.; Cournapeau, D.; Brucher, M.; Perrot, M.; Duchesnay, E. Scikit-Learn: Machine Learning in {P}ython. *J. Mach. Learn. Res.* **2011**, *12*, 2825–2830.

(31)   The GPyOpt authors. {GPyOpt}: A Bayesian Optimization Framework in Python. 2016.

(32)   Lundberg, S. M.; Lee, S. I. A Unified Approach to Interpreting Model Predictions. *Adv. Neural Inf. Process. Syst.* **2017**, *2017-Decem* (Section 2), 4766–4775.

(33)   Plotly Technologies Inc. Collaborative Data Science. Plotly Technologies Inc.: Montreal, QC 2015.

(34)   Mortensen, J. J.; Hansen, L. B.; Jacobsen, K. W. Real-Space Grid Implementation of the Projector Augmented Wave Method. *Phys. Rev. B* **2005**, *71* (3), 35109. https://doi.org/10.1103/PhysRevB.71.035109.

(35)   Enkovaara, J.; Rostgaard, C.; Mortensen, J. J.; Chen, J.; Dułak, M.; Ferrighi, L.; Gavnholt, J.; Glinsvad, C.; Haikola, V.; Hansen, H. A.; Kristoffersen, H. H.; Kuisma, M.; Larsen, A. H.; Lehtovaara, L.; Ljungberg, M.; Lopez-Acevedo, O.; Moses, P. G.; Ojanen, J.; Olsen, T.; Petzold, V.; Romero, N. A.; Stausholm-Møller, J.; Strange, M.; Tritsaris, G. A.; Vanin, M.; Walter, M.; Hammer, B.; Häkkinen, H.; Madsen, G. K. H.; Nieminen, R. M.; Nørskov, J. K.; Puska, M.; Rantala, T. T.; Schiøtz, J.; Thygesen, K. S.; Jacobsen, K. W. Electronic Structure Calculations with {GPAW}: A Real-Space Implementation of the Projector Augmented-Wave Method. *J. Phys. Condens. Matter* **2010**, *22* (25), 253202. https://doi.org/10.1088/0953-8984/22/25/253202.

(36)   Hammer, B.; Hansen, L. B.; Nørskov, J. K. Improved Adsorption Energetics within Density-Functional Theory Using Revised Perdew-Burke-Ernzerhof Functionals. *Phys. Rev. B - Condens. Matter Mater. Phys.* **1999**, *59* (11), 7413–7421. https://doi.org/10.1103/PhysRevB.59.7413.

(37)   Larsen, A. H.; Mortensen, J. J.; Blomqvist, J.; Castelli, I. E.; Christensen, R.; Dułak, M.; Friis, J.; Groves, M. N.; Hammer, B.; Hargus, C.; Hermes, E. D.; Jennings, P. C.; Jensen, P. B.; Kermode, J.; Kitchin, J. R.; Kolsbjerg, E. L.; Kubal, J.; Kaasbjerg, K.; Lysgaard, S.; Maronsson, J. B.; Maxson, T.; Olsen, T.; Pastewka, L.; Peterson, A.;

Rostgaard, C.; Schiøtz, J.; Schütt, O.; Strange, M.; Thygesen, K. S.; Vegge, T.; Vilhelmsen, L.; Walter, M.; Zeng, Z.; Jacobsen, K. W. The Atomic Simulation Environment{\textemdash}a Python Library for Working with Atoms. *J. Phys. Condens. Matter* **2017**, *29* (27), 273002. https://doi.org/10.1088/1361-648x/aa680e.

(38) Stephens, I. E. L.; Bondarenko, A. S.; Grønbjerg, U.; Rossmeisl, J.; Chorkendorff, I. Understanding the Electrocatalysis of Oxygen Reduction on Platinum and Its Alloys. *Energy and Environmental Science*. 2012. https://doi.org/10.1039/c2ee03590a.

(39) Pedersen, J. K.; Batchelor, T. A. A.; Yan, D.; Skjegstad, L. E. J.; Rossmeisl, J. Surface Electrocatalysis on High-Entropy Alloys. *Curr. Opin. Electrochem.* **2021**, *26*, 100651. https://doi.org/https://doi.org/10.1016/j.coelec.2020.100651.

(40) Quinson, J.; Simonsen, S. B.; Kuhn, L. T.; Kunz, S.; Arenz, M. Size Effect Studies in Catalysis: A Simple Surfactant-Free Synthesis of Sub 3 Nm Pd Nanocatalysts Supported on Carbon. *RSC Adv.* **2018**, *8* (59). https://doi.org/10.1039/c8ra06912c.

(41) Quinson, J. Colloidal Surfactant-Free Syntheses of Precious Metal Nanoparticles for Electrocatalysis. *Curr. Opin. Electrochem.* **2022**, *34*, 100977. https://doi.org/10.1016/J.COELEC.2022.100977.

(42) Quinn, M.; Mills, G. Surface-Mediated Formation of Gold Particles in Basic Methanol. *J. Phys. Chem.* **1994**, *98* (39), 9840–9844. https://doi.org/10.1021/j100090a018.

(43) Bizzotto, F.; Quinson, J.; Schröder, J.; Zana, A.; Arenz, M. Surfactant-Free Colloidal Strategies for Highly Dispersed and Active Supported IrO2 Catalysts: Synthesis and Performance Evaluation for the Oxygen Evolution Reaction. *J. Catal.* **2021**. https://doi.org/10.1016/J.JCAT.2021.07.004.

(44) Bizzotto, F.; Quinson, J.; Zana, A.; Kirkensgaard, J. J. K.; Dworzak, A.; Oezaslan, M.; Arenz, M. Ir Nanoparticles with Ultrahigh Dispersion as Oxygen Evolution Reaction (OER) Catalysts: Synthesis and Activity Benchmarking. *Catal. Sci. Technol.* **2019**, *9* (22), 6345–6356. https://doi.org/10.1039/c9cy01728c.

(45) Lundberg, S. M.; Erion, G.; Chen, H.; DeGrave, A.; Prutkin, J. M.; Nair, B.; Katz, R.; Himmelfarb, J.; Bansal, N.; Lee, S.-I. From Local Explanations to Global Understanding with Explainable AI for Trees. *Nat. Mach. Intell.* **2020**, *2* (1), 2522–5839.

(46) Papandrew, A. B.; Atkinson, R. W.; Unocic, R. R.; Zawodzinski, T. A. Ruthenium as a CO-Tolerant Hydrogen Oxidation Catalyst for Solid Acid Fuel Cells. *J. Mater. Chem. A* **2015**, *3* (7), 3984–3987. https://doi.org/10.1039/c4ta06451h.

(47) Lai, S. C. S.; Lebedeva, N. P.; Housmans, T. H. M.; Koper, M. T. M. Mechanisms of Carbon Monoxide and Methanol Oxidation at Single-Crystal Electrodes. *Top. Catal.* **2007**, *46* (3–4), 320–333. https://doi.org/10.1007/s11244-007-9010-y.

(48) Rodriguez, P.; Koper, M. T. M. Electrocatalysis on Gold. *Phys. Chem. Chem. Phys.* **2014**, *16* (27), 13583–13594. https://doi.org/10.1039/c4cp00394b.

(49) Goyal, A.; Marcandalli, G.; Mints, V. A.; Koper, M. T. M. Competition between CO_2 Reduction and Hydrogen Evolution on a Gold Electrode under Well-Defined Mass Transport Conditions. *J. Am. Chem. Soc.* **2020**, *142* (9), 4154–4161. https://doi.org/10.1021/jacs.9b10061.

(50) James, G.; Witten, D.; Hastie, T.; Tibshirani, R. *Linear Model Selection and Regularization*; Springer Texts in Statistics; Springer New York: New York, NY. https://doi.org/10.1007/978-1-4614-7138-7.

(51) Lin, W. F.; Zei, M. S.; Eiswirth, M.; Ertl, G.; Iwasita, T.; Vielstich, W. Electrocatalytic Activity of Ru-Modified Pt(111) Electrodes toward CO Oxidation. *J. Phys. Chem. B* **1999**, *103* (33), 6968–6977. https://doi.org/10.1021/jp9910901.

(52) Gasteiger, H. A.; Markovic, N.; Ross, P. N.; Cairns, E. J. CO Electrooxidation on Well-Characterized Pt-Ru Alloys. *J. Phys. Chem.* **1994**, *98* (2), 617–625. https://doi.org/10.1021/j100053a042.